Research Article Vol. 39, No. 10 / October 2022 / Journal of the Optical Society of America B 2573

Journal of the Optical Society of America B

OPTICAL PHYSICS

Technique for improving polarization conversion performance

YUPENG LI, LI ZENG, AND HAIFENG ZHANG*

College of Electronic and Optical Engineering & College of Flexible Electronics (Future Technology), Nanjing University of Posts and Telecommunications, Jiangsu Province 210023, China
**Corresponding author: hanlor@163.com*

Received 13 June 2022; revised 6 August 2022; accepted 17 August 2022; posted 18 August 2022; published 6 September 2022

In this paper, a novel technology based on the addition of air through-hole structures (ATSs) is proposed to optimize the performance of polarization conversion. Based on the tree-shaped resonator (patch), the working band can be moved and widened by adding the ATS with a certain radius. Among them, in terms of a theorem, angular stability, parameters, and so on, the detailed analysis of the metasurface whose ATS radius is 5 μm is presented. Apart from this, to highlight the superiority and the role of the ATS, the metasurface without ATS is also discussed identically as above. To be specific, due to the addition of ATS, the two original narrowbands, which are operating at 0.725–1.013 THz and 1.225–1.423 THz (polarization conversion rate >90%), are widened into a complete broadband (0.90–1.86 THz). In this case, the metasurface with ATS possesses a relative bandwidth of 69.6%. When the linearly polarized wave is irradiated vertically on the metasurface, the electric field orientation of the wave is converted by 90° from the *x* axis to the *y* axis. Therefore, the metasurface holds promising applications in radar, communications, and so on. © 2022 Optica Publishing Group

https://doi.org/10.1364/JOSAB.467682

1. INTRODUCTION

In recent years, the electromagnetic wave (EMW) has made significant breakthroughs in theories and considerable signs of progress in applications. The theories of EMW have played a pivotal role in optical imaging, wireless communication, etc. [1–3]. As a significant phenomenon of EMW, polarization has triggered research and discussions extensively and enthusiastically. Thus, the polarization converter that can transform the phase and amplitude of the EMW is put forward [4,5]. To ensure that the incident light travels a sufficient distance in the optical medium, the conventional polarization converters based on the Brewster effect and the birefringence principle are generally bulky in size [6–8]. Moreover, it is accompanied by the drawbacks of limited media for polarization regulation, narrow working band, and low conversion efficiency [9,10]. In pace with the continuous improvement in science and technology, the development requirements such as microminiaturization and integration are no longer satisfied [11]. However, the emergence of artificial metamaterials overcomes the above-mentioned shortcomings, which establish the basis for the development of miniaturization and integration of devices [12,13].

Metamaterials are artificial materials that are arranged and combined with subwavelength structures as the basic units [14–16]. Generally speaking, by adjusting the size and shape of the basic unit, some physical properties that are non-existent in natural materials, such as refractive index and permittivity being negative, can be achieved [17–19]. Among them, the two-dimensional metamaterials are known as metasurfaces, planar metamaterial consisting of subwavelength plasmonic or dielectric structures [20], which are extensive in usage [10,21,22]. On account of the aforementioned merits, the polarization conversion devices are combined with metasurfaces to carry out innovative designs [23–25]. Afterward, the designs of polarization conversion metasurfaces have emerged endlessly.

Specific examples can be searched. A reflective metasurface project provided with polarization conversion function was proposed by Zhou's research group in 2007 [26]. The device possesses a three-tier structure, which can attain an excellent polarization conversion effect at both 6.8 GHz and 12.7 GHz. A rectangular resonant surface with an inclination angle of 45° in 2013 was proposed by Grady *et al*. The results of the full-wave numerical simulations show that the cross-polarized reflection is higher than 80% and the co-polarized reflection is lower than 5% between 0.8 THz and 1.36 THz. Based on the above-mentioned structure, a grating structured metasurface has also been proposed, which allows perfect anomalous refraction [27]. In the following year, replacing metallic resonant patches with plasma for a super-surface was proposed by Yang *et al*. Theoretically, the structure provides over a 98% polarization conversion rate (PCR) in the short-wavelength infrared band over 200 nm bandwidth. However, the material has certain limitations when it comes to fabrication [28]. In 2016, the metasurface with asymmetric cross-shaped resonant

structure [29] advanced by Zhang *et al*. was no longer confined to single-frequency or multi-frequency operation. Specifically, this metasurface possesses a PCR of over 80% in the 8.3–14.3 GHz band with a relative bandwidth (RB) of 53.1%. In addition, in 2018, Zhao *et al*. [30] proposed a kind of metasurface whose metal split rings nested outside the metal circularity. In the band range of 0.65–1.58 THz, this design achieves a PCR greater than 80% without a pump beam. In 2019, the T-shaped resonant metasurface designed by Ako *et al*. achieved more than 80% PCR and the broadband effect at both normal and 45° incidence of EMWs [31]. Such polarized metasurfaces have come out in an unending flow. However, some obvious shortcomings remain in the polarization conversion metasurfaces described above. Generally speaking, when the metasurfaces feature a high PCR, the operating range is multifrequency or narrowband, while when the metasurfaces possess the broadband effect, the PCR is usually guaranteed to be above 80%. Therefore, some novel optimizations are required for a polarization conversion metasurface to have both broadband effect and high PCR.

In 2020, a cross-polarization converter designed by our team [32] gained a superior PCR while achieving an ultra-wideband effect. Eventually, the goal for the PCR to surpass 90% in the working band of 0.63–1.50 THz was achieved. Additionally, this paper proposes a reliable method (the addition of the second layer resonant structure) to optimize the performance indicators such as bandwidth, PCR, and angular stability of the metasurface, and a detailed comparison of the design before and after optimization was performed. The following year, our team also proposed a method to broaden the operating band by combining four units with similar structures but different parameters [33]. This method enables the combined structure to achieve a polarization conversion function in 0.91–1.67 THz with the RB superior to that of the four units. Huang *et al*. in 2021 also proposed a kind of metasurface to achieve band broadening by multi-layered design. With composite pulse control, the bandwidth (PCR > 90%) is expanded by 201% compared to the single-layer structure when the number of multi-layers reaches 7 [34]. The above-mentioned papers furnish novel ideas for the realization of ultra-broadband and high PCR indicators of polarization conversion metasurfaces. However, the above methods also have certain drawbacks. The stacking and combination of structures create larger cross sections.

In recent years, air cavity structures by specific design have received mentions in bandwidth expansion and performance optimization. In 2018, Liu *et al*. designed a metasurface unit with a perforated structure [35]. When the original absorption peak and the size of the structure remain unchanged, the structure produces a new near-perfect absorption peak at high frequencies, thus enabling a multi-order absorption mechanism. Zhang *et al*. designed an absorber in combination with the air cavity structure in 2020 [36]. The simulation results show that the working band is broadened and somewhat blueshifted (from 4.65–8.86 THz to 5.35–13.08 THz) when the cavity structure is added. In addition, the air cavity structures and their complementary dielectric metasurfaces are also used in many types of devices. Armelles *et al*. discussed the magnetic field correction for photomagnetic dipoles using Barbier's principle [37]. Using the complementary dielectric metasurface with the air cavity structures, a broadband unpolarized terahertz beam splitter designed by Wei *et al.* [20] and Magnusson *et al.* [38] reviewed guided-mode resonant photonic lattices by addressing their functionalities and potential device applications. However, the use of air cavity structures in the design of polarization converters to enhance the PCR and expand bandwidth is almost unheard of. Therefore, the air cavity structures have left undeveloped application fields in the polarization conversion metasurfaces of polarization detection, antennas, imaging, and optical communication [39].

Under the condition that the resonant surface structure does not alter, a means to optimize performance indicators such as bandwidth and PCR by adding air through-hole structures (ATSs) will be discussed in this paper. The described ATS optimization technique will significantly constrain more electric fields on the metal resonator, which enhances the magnetic resonance strength along the diagonal direction so that more of the incident field energy will be converted by the metal structure into its cross-polarized form and be reflected. In addition, the introduction of ATS will also bring additional cavity resonances. In the coupling with the magnetic resonances, it will further help in broadening the bandwidth and PCR. In this paper, a kind of metasurface with a tree-shaped metal resonant patch has been proposed for illustration. The simulation reveals that the bandwidth whose PCR is higher than 80% ranges from 0.72 to 1.42 THz. However, when aspiring for more than 90% PCR, the operating band is curtailed to two narrowbands of 0.725–1.015 THz and 1.225–1.423 THz. After that, a certain number of ATS are designed in the intermediate dielectric layer. By adjusting the radius of the ATS, it is easy to optimize the PCR and the broadening and shifting of the operating band.

2. THEORETICAL MODEL

Simulations of the designs are carried out in HFSS, a commercially available three-dimensional (3D) structural EMW simulation software. By placing the boundary conditions on the master-slave, the arrangement of the boundless period can be accomplished. At a certain distance directly above the resonant unit, the Floquet port is provided to guarantee that the polarization direction of the EMW is along the x axis.

Structurally, the unit of the proposed metasurface consists of a resonator layer on the top and a reflector on the bottom, which are separated by an intermediate dielectric substrate. The reflective and resonant layers are gold with an electrical conductivity of 4.561×10^7 s/m [40], while the intermediate dielectric layer is made of glass plates (normal lossy) with a dielectric constant stable at 4.82 [41]. A further explanation of this structural unit ensues in detail. The structural unit, notably the surface resonant structure, is overall axisymmetric along the u axis [the u axis deviated from the x axis by 45° as shown in Fig. 1(b)]. The top resonator resembles the shape of a tree, the "leaf" part of which is formed by cutting two circular structures (radius set to b) from a rectangle and connecting it to a rectangular "trunk" with the length and width of l and e. For this unit, the ATS is a plurality of cylindrical air cavities formed by scooping out the cylindrical structures from the intermediate dielectric layer. The distance between the two through-holes is set as parameter x. Besides, the radius of the through-holes is

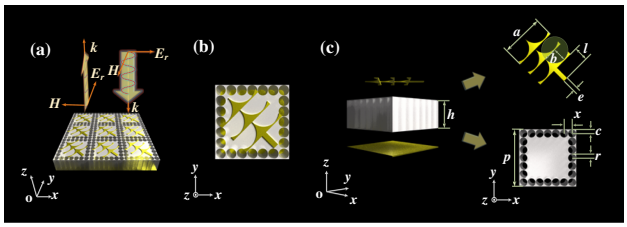

Fig. 1. Diagrams of the polarization converter in various angular versions: (a) periodic array diagram (3 × 3); (b) overhead view; (c) separated schematic diagrams of the three-tier structure.

Table 1. Characterization Parameters of the Designed Polarization Conversion Unit with the Specific Values

Parameters	h	d	p	a
Value (μm)	30	0.3	70	24
Parameters	r_1	l	e	x
Value (μm)	16	16	2.4	10
Parameters	c	r		
Value (μm)	5	5		

set as r, whose value can be varied somewhat depending on the desired bandwidth or other performance indicators. Figure 1(c) also reveals several significant pieces of information regarding the cell dimensions, whereby the cell length $p = 70$ μm, the thickness of the dielectric layer $h = 30$ μm, and the thickness of the metal part $d = 0.3$ μm. All information about structure can be summed up explicitly from Fig. 1, which shows the 3D views of the described polarization converter unit and periodic array. Furthermore, more about the parameter values in detail is given in Table 1.

3. ANALYSIS AND DISCUSSION

When analyzing the principle of polarization conversion, several requisite variables are required to be defined and discussed. First of all, when the incident polarized EMW (the electric field is along the x axis) propagates along the line of the z axis typically, the cross-polarized reflected coefficient is represented by r_{yx}, and the co-polarized reflected coefficient is written as r_{xx}. Similarly, the cross-polarized and co-polarized transmitted coefficients can be denoted as t_{yx} and t_{xx}, separately. At this point, the PCR, one of the most significant indicators to measure the effect of polarization conversion, is calculated by the following formula [28]:

$$\mathrm{PCR} = \frac{r_{yx}^2}{r_{yx}^2 + r_{xx}^2 + t_{yx}^2 + t_{xx}^2}. \tag{1}$$

Nevertheless, when the bottom layer of the structure is designed as a metal plate, the transmitted wave is cut off. Thus, the PCR equation changes to the following form [28]:

$$\mathrm{PCR} = \frac{r_{yx}^2}{r_{yx}^2 + r_{xx}^2}. \tag{2}$$

According to the law of conservation for energy, $r_{yx}^2 + r_{xx}^2$ will infinitely converge to 1 in the lossless case. Thus, by transforming Eq. (2), we get $\mathrm{PCR} = 1 - r_{xx}^2 = r_{yx}^2$. Typically, the operating bands or frequency points where the PCR exceeds 0.9 are of value. Converting the criterion of PCR > 0.9 into the reflected coefficient is expressed as

$$|r_{xx}| \le -10\ \mathrm{dB}. \tag{3}$$

Second, when the incident polarization direction of the EMW is along the u axis, the co-reflection amplitude is denoted as $|r_{uu}|$. Meanwhile, the co-reflection coefficients when the above direction is along the v axis are defined as $|r_{vv}|$. The corresponding reflected coefficients are expressed as

$$\boldsymbol{r}_{uu} = |\boldsymbol{r}_{uu}|\, \boldsymbol{e}^{j\varphi_u}, \tag{4}$$

$$\boldsymbol{r}_{vv} = |\boldsymbol{r}_{vv}|\, \boldsymbol{e}^{j\varphi_v}. \tag{5}$$

In the case of lossless cross-polarized conversion, the values of those amplitudes above are close to 1 [8]. (Since most of the resonant surfaces designed to implement the polarization conversion function are mirror-symmetric along the u and v axes, $\boldsymbol{r}_{uv}$ and $\boldsymbol{r}_{vu}$ are both suppressed to 0.) φ_u and φ_v are the co-polarized reflected phases. Then, the reflected wave Eq. (7) can be derived from the incident EMW in Eq. (6) combined with the definitions of Eqs. (4) and (5) as follows:

$$\vec{E}_{\mathrm{inc}} = E_0(\hat{u} + \hat{v})/\sqrt{2}, \tag{6}$$

$$\vec{E}_{\mathrm{ref}} = E_0\left[\hat{u}e^{j\varphi_u} + \hat{v}e^{j\varphi_v}\right]/\sqrt{2}. \tag{7}$$

We convert the u and v variables to x and y axis variables according to the following rules:

$$\hat{u} = (\hat{x} + \hat{y})/\sqrt{2}, \tag{8}$$

$$\hat{v} = (\hat{y} - \hat{x})/\sqrt{2}. \tag{9}$$

Bringing Eqs. (8) and (9) into Eq. (7), the reflected wave expression in terms of x and y vectors can be attained:

$$\vec{E}_{\mathrm{ref}} = \frac{E_0}{2}\left[\hat{x}(e^{j\varphi_u} - e^{j\varphi_v}) + \hat{y}(e^{j\varphi_u} + e^{j\varphi_v})\right]. \tag{10}$$

At this point, based on the reflected wave Eq. (10), the cross-polarized reflected coefficient and co-polarized reflected coefficient are defined by the following specific formulas:

$$\boldsymbol{r}_{xx} = \frac{\boldsymbol{e}^{j\varphi_u} + \boldsymbol{e}^{j\varphi_v}}{2}, \tag{11}$$

$$\boldsymbol{r}_{yx} = \frac{\boldsymbol{e}^{j\varphi_u} - \boldsymbol{e}^{j\varphi_v}}{2}. \tag{12}$$

We solve Eq. (3) in conjunction with Eq. (11), while defining phase difference $\Delta\varphi = \varphi_u - \varphi_v$. Ultimately, it is clear to know that the evaluation criterion of PCR > 0.9 is met when the phase difference condition satisfies Eq. (10):

$$180^\circ - 37^\circ \le |\Delta\varphi| \le 180^\circ + 37^\circ. \tag{13}$$

The equations above [31,42] are the derivations of the relevant theorems for polarization conversion. The subsequent

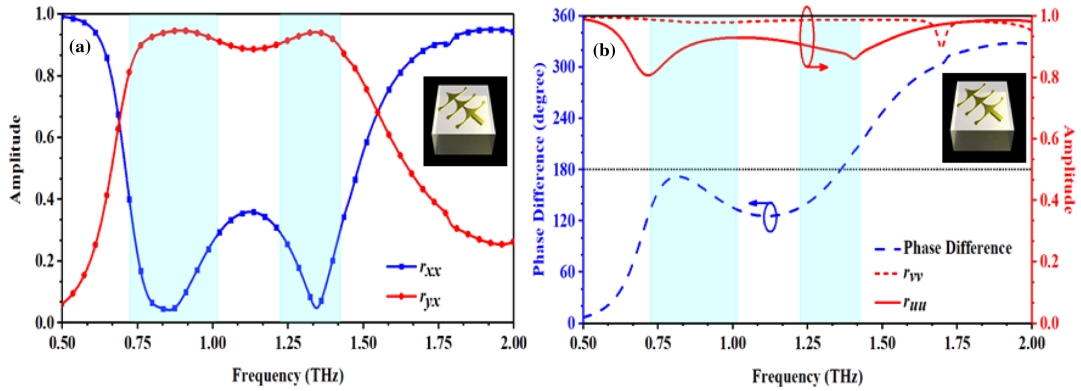

Fig. 2. (a) Reflected amplitudes in co-polarization (r_{xx}) and cross-polarization (r_{yx}) under the normal incidence of an x-polarized wave, and (b) the co-polarized reflected amplitudes and the phase difference under the normal incidence of u-and v-polarized waves of the metasurface without ATS.

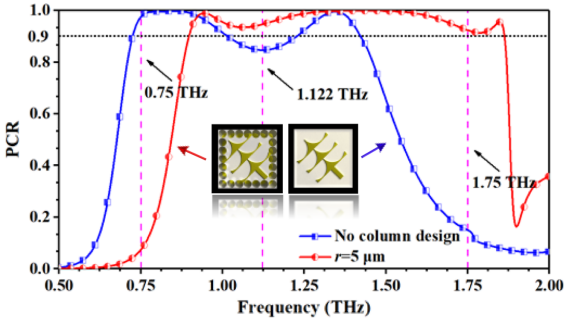

Fig. 3. Schematic diagram of the PCR curves of the designed polarization conversion metasurface in two structures.

is the specific numerical analysis of the proposed metasurface in this paper. It should be noted that the blue areas in Figs. 2 and 3 mark the operating band (PCR > 0.9) of the respectively described metasurfaces.

Simultaneous adjustment of amplitude and phase is necessary if the propagation of EMWs is to be fully controlled [42]. The polarization conversion metasurface without ATS is investigated at first. The information depicted in Fig. 2 is about the reflected coefficients. As observed in Fig. 2(a), the amplitude of the cross-reflected coefficient is represented by the blue line, which increases significantly and approaches 1 in the range of 0.725–1.423 THz. In contrast, the amplitude of the co-polarized reflected coefficients indicated by the red line decreases rapidly. Nonetheless, this tendency is somewhat weakened between 1.013 and 1.225 THz. Within this frequency range, r_{yx} decreases but not significantly, and the curve reaches its lowest point at 1.122 THz with an amplitude of 0.887. However, the value of r_{xx} increases rapidly and no longer approaches the 0 reference line, reaching a value close to 0.4. By observing Fig. 2(b), the reflection amplitude and phase difference trends can be obtained for u- and v-polarized waves, respectively. The two reflection amplitude curves in Fig. 2(b) exhibit a mutual fit, which satisfies the condition that the two values are almost equal. (Due to the ohmic loss of the metal resonator and the loss tangent of the dielectric substrate, the fit of the curves is approximate at terahertz frequencies [43].) The phase difference in the 0.725–1.013 THz and 1.225–1.423 THz bands fulfills Eq. (13). From a phase point of view, the PCR is guaranteed to be above 90% in the above two bands. The above description is calculated by the PCR equation and plotted as the blue curve in Fig. 3. In the two operating bands (0.725–1.013 THz and 1.225–1.423 THz), it can be obviously seen that the PCR closes to the reference line 1 virtually, which reflects the superior polarization conversion effect. In contrast, in 1.013–1.225 THz, the PCR is less than 0.9 and possesses a certain polarization conversion capability. Therefore, the improvement of the above-mentioned band is the optimization target.

The modification is based on the use of the ATS technique. Precisely, a certain number and radius of ATS are placed at the edge of the intermediate media layer, as described in the "Theoretical Model" unit. Here only one case with the holes radius of 5 μm is discussed in depth. By comparing the curve of r_{xx} in Fig. 2(a) with that in Fig. 4(a), one noticeable difference is that, in the "Linear" mode, two resonant frequency points (located initially at 0.848 THz and 1.345 THz) have been increased to three after optimization. Notably, the resonant point at 1.41 THz impacts a wide range, which keeps the co-polarized reflection amplitude surrounding this point at a low value. As is known, the number of resonant frequency points increases and remains somewhat close to each other, both of which are conducive to the formation of the ultra-broadband effect. Meanwhile, the r_{yx} remains smooth and approaches the value of 1 in 0.90–1.86 THz. Furthermore, at the ATS radius of 5 μm, the phase difference curve fits more continuously and tightly to the 180° standard line, as demonstrated by the blue dashed lines in Fig. 4(b). While the curves of r_{uu} and r_{vv} are consistent with the previous trend, both fit each other and satisfy the conditions when the polarization conversion happens. Likewise, the above variations and improvements are evident, as can be noticed from the red curve in Fig. 3. Ultimately, the PCR is maintained above 90% within 0.90–1.86 THz.

The surface current distributions of the resonant unit without and with ATS at 1.122 THz are depicted in Fig. 5, separately. The reason why the frequency point at 1.122 THz has been chosen is to better emphasize and illustrate the optimizing effect of the ATS as exhibited in Fig. 3. Since the current trends are essentially the same for both structures at 1.122 THz, the analysis will focus on the unit with ATS as shown in Figs. 5(c) and 5(d). The current trends for each branch of the top resonant patches

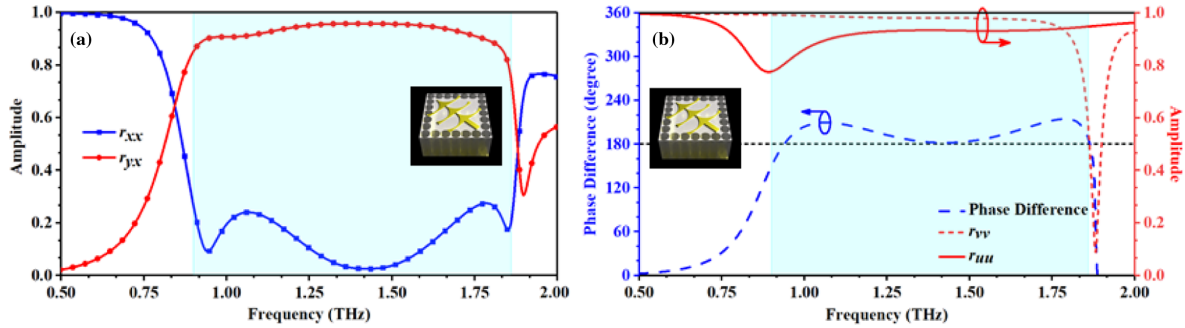

Fig. 4. (a) Reflected amplitudes in co-polarization (r_{xx}) and cross-polarization (r_{yx}) under the normal incidence of x-polarized wave, and (b) the co-polarized reflected amplitudes and the phase difference under the normal incidence of u-and v-polarized waves of the metasurface with ATS.

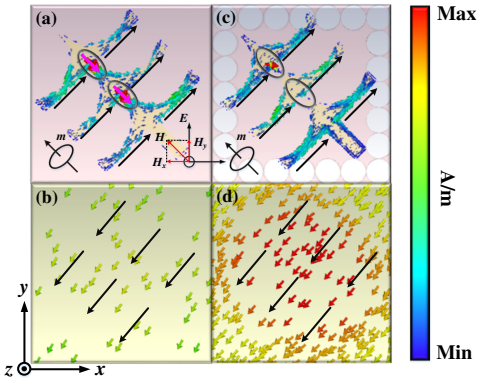

Fig. 5. Current distribution at 1.122 THz: (a) on the top resonant patches without ATS, (b) on the bottom metal reflector without ATS, (c) on the top resonant patches with ATS, and (d) on the bottom metal reflector with ATS.

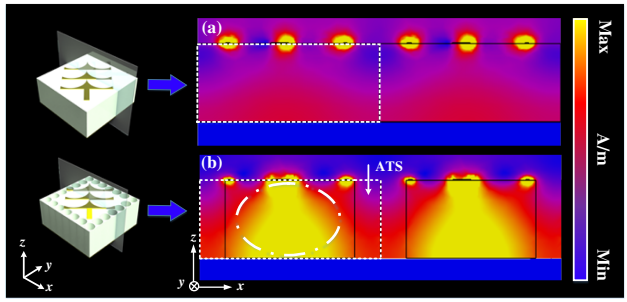

Fig. 6. Magnetic field distribution in the xoz plane at 1.122 THz: (a) metasurface without ATS; (b) metasurface with ATS.

are indicated by the black arrows. The currents on the bottom metal reflector are expressed by the same method as above. The currents in the upper and bottom layers are in opposite orientations, thus forming a circulation in the intermediate dielectric layer, which is in accordance with the right-hand rule and is generated the magnetic dipole $\boldsymbol{m}$. The corresponding magnetic field $\boldsymbol{H}$ is oriented along the $-u$ axis, which can be decomposed into the xoy coordinate axis, i.e., $\boldsymbol{H}_x$ and $\boldsymbol{H}_y$. Among them, the magnetic field component $\boldsymbol{H}_y$, which is parallel to the direction of the electric field ($\boldsymbol{E}$), results in the polarization conversion from an x-polarized wave to a y-polarized wave. Moreover, it can be observed that the current density and intensity vary due to the addition of ATS. For the metasurface without ATS, some current components along the positive direction of the u axis are at the connections of the top resonant patch, as indicated by the pink arrows in Fig. 5(a). They are useless for the formation of circulating currents. However, these unwanted current components are weakened after adding the ATS, as displayed in Fig. 5(b). In addition, by comparing Figs. 5(b) and 5(d), it can be noticed that the addition of the ATS results in more concentrated and more robust current distributions on the bottom metal reflector.

However, the phenomenon of magnetic resonance enhancement due to ATS can also be well reflected in the magnetic field distribution in the xoz plane. The strong magnetic field distribution can be found on all the metal resonant patches under the cross section by setting the observation section at the center of the length of the unit. (It should be noted that, since the currents outlined in the circles in Figs. 5(a) and 5(c) are not participating in the magnetic resonance, their variation will not be represented in the magnetic field distribution in the xoz plane.) When the metasurface is without ATS, as shown in Fig. 6(a), the magnetic field distribution is present in the intermediate dielectric layer and affects the metal reflector uniformly, which is significantly enhanced and converged due to the addition of the ATS, as indicated in Fig. 6(b). The above-described phenomenon can also be seen in the comparison between Figs. 5(b) and 5(d).

The described ATS optimization technique will significantly constrain more electric fields on the metal resonator, which enhances the magnetic resonance strength along the diagonal direction so that more of the incident field energy will be converted by the metal structure into its cross-polarized form and be reflected. In addition, the introduction of ATS will also bring additional cavity resonances. In the coupling with the magnetic resonances, it will further help in broadening the bandwidth and PCR. For further visualization, the pictures of the electric field distribution are introduced in Fig. 7. Figure 7(a) reveals that the more active parts of the electric field are mainly concentrated in areas 2 and 3 of the "tree" structure. Areas 1 and 4 marked in the diagram show the comparatively weak state of the electric field strength. However, for the unit with ATS, as displayed in Fig. 7(b), the electric field intensity in the regions 5 and 8 corresponding to the regions 1 and 4 are enhanced, and the color changes from the previous yellow to red. Therefore, it can be concluded that the effect of polarization conversion has

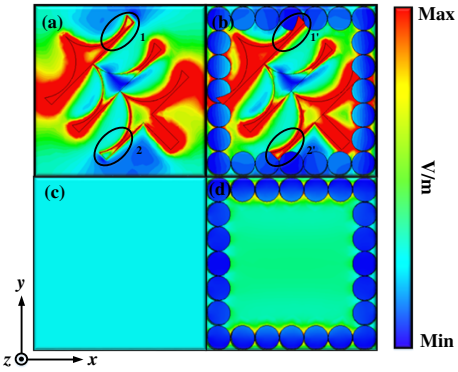

Fig. 7. Electric field distribution of the metasurface at 1.122 THz: (a) without ATS and (b) with ATS. Electric field distribution in the presence of the dielectric layer and the metal reflector only: (c) without ATS and (d) with ATS.

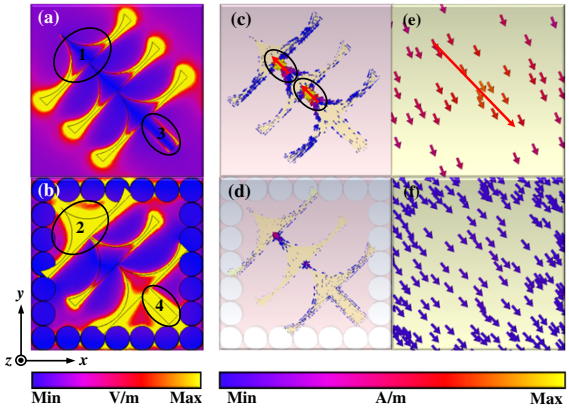

Fig. 8. Electric field distribution at 0.75 THz: (a) without ATS, (b) with ATS. Current distribution at 0.75 THz: (c) on the top resonant patches without ATS, (d) on the bottom metal reflector without ATS, (e) on the top resonant patches with ATS, and (f) on the bottom metal reflector with ATS.

been improved due to the localized enhancement phenomenon of the electric fields. The individual analysis of the ATS in the local enhancement of the electric field distribution at 1.122 THz is displayed in Figs. 7(c) and 7(d) when the resonant patch is removed. The electric field strength of the structure without ATS in Fig. 7(c) is approximately 1.5×10^5 V/m. However, in Fig. 7(d), the electric field intensity in the regions surrounded by the ATS is nearly double enhanced to approximately 2.9×10^5 V/m. Such phenomena fully demonstrate the effectiveness of ATS on near-field localization. The increase in electric field strength will lead to a further enhancement of the polarization conversion after adding the metal resonator, which is confirmed in the result of the PCR in Fig. 3. The increase in electric field strength leads to an enhancement of the operating effect (i.e., the reflection or the polarization conversion of EMWs) for the present structure at different frequencies, as displayed in Figs. 8 and 9 at 0.75 THz and 1.75 THz, respectively.

The proposed metasurfaces with and without ATS at 0.75 THz exhibit different operating states, as shown in Fig. 3,

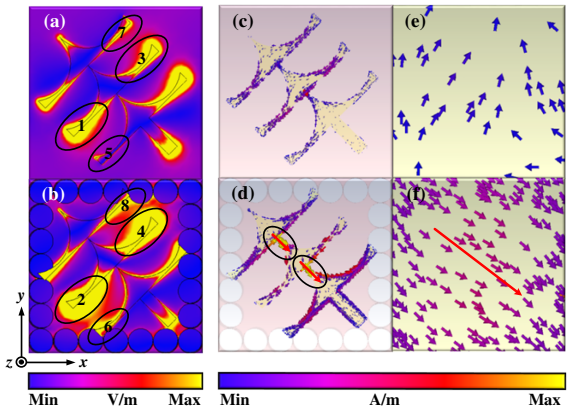

Fig. 9. Electric field distribution at 1.75 THz: (a) without ATS, (b) with ATS. Current distribution at 1.75 THz: (c) on the top resonant patches without ATS, (d) on the bottom metal reflector without ATS, (e) on the top resonant patches with ATS, and (f) on the bottom metal reflector with ATS.

i.e., the metasurface without ATS carries out the highly efficient polarization conversion while the metasurface with ATS undergoes the reflection of EMWs. As shown in Figs. 8(a) and 8(b), there are significant enhancements of the electric field at 0.75 THz in regions 1 and 3 compared to regions 2 and 4 due to the addition of the ATS, which contributes to the polarization conversion. In Figs. 8(c) and 8(d), the currents are in the opposite directions to form the loops and, thus, produce the magnetic resonances that allow for the polarization conversion. In contrast, in Figs. 8(e) and 8(f), the current distribution is too weak to generate an effective magnetic resonance, and the current density and intensity on the bottom metal reflector are significantly greater than the current on the resonant patch so that the metasurface with ATS at 0.75 THz produces the predominantly highly reflection. At this point, the ATS mainly enhances and concentrates the energy of the electric field involved in the reflection.

The situation is different at 1.75 THz. The metasurface with ATS carries out the highly efficient polarization conversion while the metasurface without ATS undergoes the reflection of EMWs. The surface currents on the metasurface without ATS are quite weak and spurious, whereas the strong currents are present on the metasurface with ATS, especially in the marked region. However, since the currents in the resonant patch and the metal reflector are parallel and in the same direction as displayed in Figs. 9(e) and 9(f), the electrical resonance occurs instead of the magnetic resonance. In addition, the electric field that is conducive to the polarization conversion is enhanced by the constraint of ATS, as indicated by the areas marked using the circles in Figs. 9(a) and 9(b). The areas with the strong electric field energy (areas 1, 3, and 7) are expanded as displayed in areas 2, 4, and 8, while area 5, where the electric field is weak, has undergone a substantial increase in the electric field energy under the action of the ATS as shown in area 6. In summary, the ATS structure concentrates and intensifies the electric field, whether the metasurface is operating at the frequency of EMW reflection or at that of polarization conversion.

In operational or natural conditions, the incident wave is not sufficiently guaranteed to be incident normally on the surface

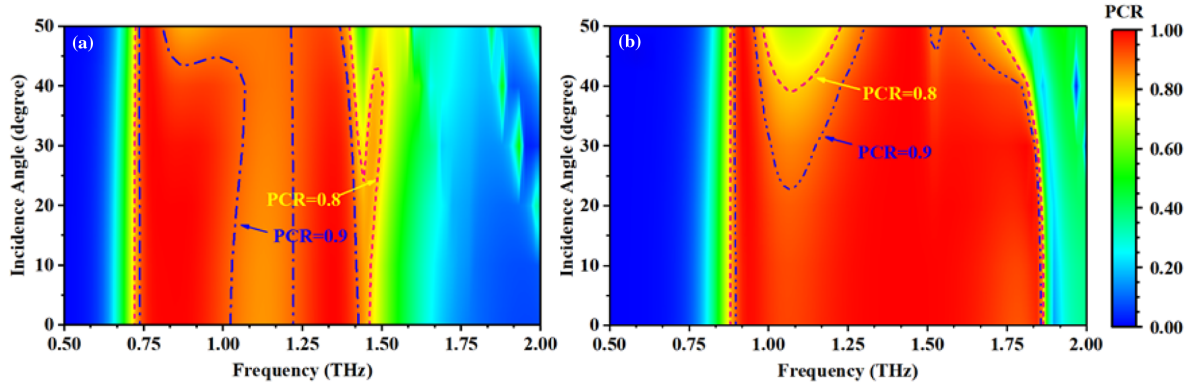

Fig. 10. Analysis of angular stability: (a) spectra of PCR for various incident angle without ATS; (b) spectra of PCR for various incident angle with ATS.

of the device, which is why the angular stability of the device is exceptionally critical. A comparison of the angular stability will be conducted here between the metasurface without and with ATS ($r = 5$ μm). Figure 10(a) delineates the angular stability of the metasurface without ATS, and the red and blue dashed lines label the areas of PCR > 0.8 and PCR > 0.9 separately. First of all, the bandwidth of PCR > 0.8 remains essentially constant when the incidence angle is altered from 0° to 50°. Even a new resonance point is isolated from 23° to 42°. All of the above are excellent, and it tentatively indicates that the metasurface without ATS has a certain angular stability. Furthermore, the two narrowbands with PCR > 0.9 vary marginally at incidence angles of less than 43°. In detail, the narrowband at 0.725–1.013 THz widens, and the operating band at 1.225–1.423 THz becomes narrower progressively and slightly. However, at incidence angles over 43°, the original 0.725–1.013 THz band shrinks promptly.

The variation of the PCR on the metasurface after the addition of ATS is observed in Fig. 10(b) when the incidence angle changes. The operating band in the 0.90–1.86 THz maintains stability when illuminating incident light at less than 23°. Yet, at more than 23°, a deterioration of the PCR exists at 1.07 THz. It means that, at 1.07 THz, the ability of polarization conversion continuously diminishes as the incidence angle continues to rise. The value of PCR is not only lower than 0.9 at 23° but also less than 80% at 40°. Moreover, the range affected by the deterioration of the above-mentioned frequency point is gradually widened. Simultaneously, a slight constriction of the frequency range at high frequencies is noted at incidence angles exceeding 40°.

The discussion of structure parameters is essential. Hence, the radius r of the ATS, which most highlights the ATS technique, is adopted for discussion here. To start with, when $r = 3$ μm, three resonant frequencies exist at 0.833 THz, 0.987 THz, and 1.405 THz, respectively. The frequency originally situated at 0.833 THz gradually blueshifts with the increase of r. When the radius reaches 5 μm, this point has moved to 0.942 THz (as marked in sign ①). The same trend occurs at the frequency point initially placed at 0.987 THz. The slight difference is that the blueshifts for this frequency are somewhat stronger and shift to 1.245 THz as soon as r reaches 4.5 μm [as illustrated by the purple dashed line in Fig. 11(b)]. At $r = 5$ μm, what is noteworthy is that the described second frequency is amalgamated with the third one at 1.405 THz, where the third frequency produces essentially no frequency shift and the r_{xx} changes from −26.299 dB to −31.375 dB (as marked in signs ② and ③). For the first two resonant points, the inconsistency in the speed of the blueshift causes the distance between the two points to grow further apart. The phenomenon means a certain degree of depression in the PCR curve occurs with the increase of r, as displayed in Fig. 11(a).

Meanwhile, a fresh resonant frequency point emerges at 1.850 THz (as marked in sign ④), which exhibits that the amplitude of r_{xx} is equal to −15.197 dB at $r = 5$ μm. According to Eq. (3) derived in the preceding section, the resonant frequency point where the amplitude of r_{xx} lies less than −10 dB is a critical factor to affect PCR > 90%. From the PCR perspective, as displayed in Fig. 11(a), the continuous raising of the last frequency point in PCR drives the interconnection between medium and high frequencies and ultimately achieves the technical target of broadening the working band. Based on the above assessment, $r = 5$ μm is chosen with the operating band of 0.90–1.86 THz.

In addition to considering the radius (r) of the ATS, subsequently, the variation in the thickness (h) of the media layer is analyzed briefly (in the case of $r = 5$ μm). Observing the evolution of the r_{xx} curves, as displayed in Fig. 11(d), one distinctive feature is that the resonance point situated around 0.94 THz decreases gradually with the increase of h. The r_{xx} at 1.84 THz conforms to a trend of first decreasing and then increasing. The above two resonance points differ in that the point at low frequencies constantly remains below −10 dB. Yet, at the high frequencies area, the r_{xx} at near 1.84 THz is above −10 dB after $h > 30$ μm. All of the foregoing is evident in the changes in the PCR curves that are shown in Fig. 11(c). Furthermore, due to the thickening of the dielectric layer, the resonance point at the mid-frequency produces a certain degree of red shift (as marked in sign ②). The broadband effect is created from resonance points close to each other. And conversely, if the two resonance frequencies lie far apart, the PCR curve can be somewhat concave. Thus, broadening the operating band can be accomplished when the resonance points are at appropriate frequencies. On the basis of the above assessment, $h = 30$ μm is chosen as the best parameter with the operating band of 0.90–1.86 THz.

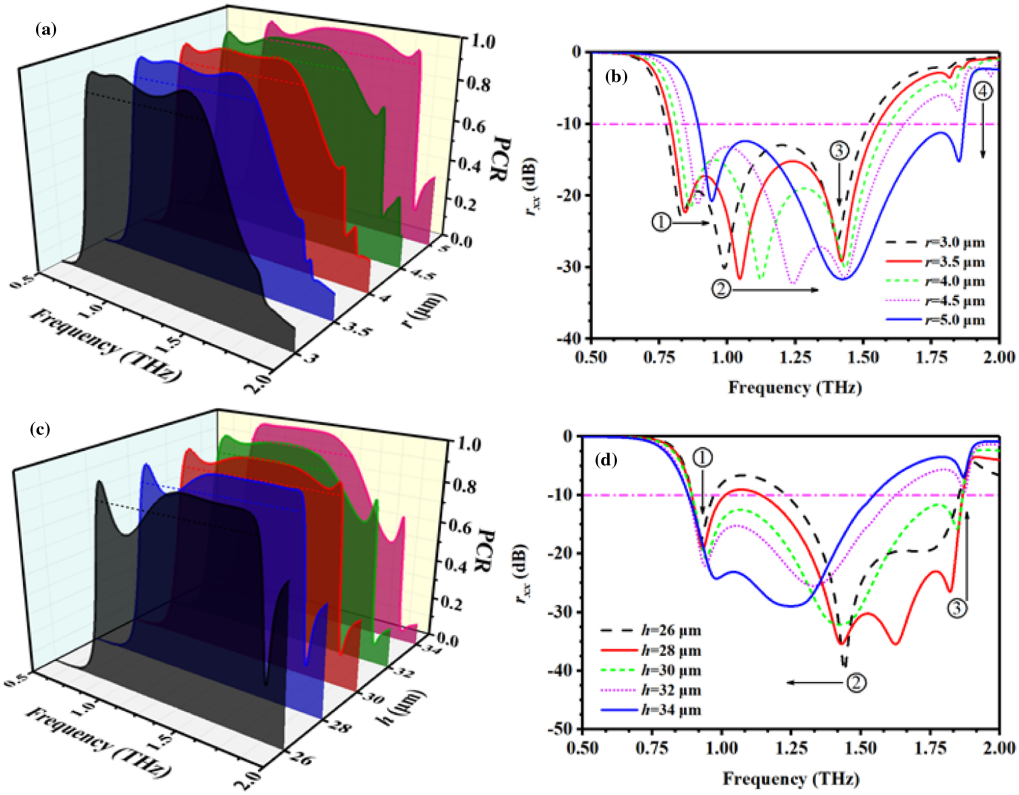

Fig. 11. PCR and co-polarized reflection amplitude (magnitude in dB) varied with different structure parameters r and h: (a) PCR varied with r, (b) co-polarized reflection amplitude varied with r, (c) PCR varied with h, and (b) co-polarized reflection amplitude varied with h.

4. CONCLUSION

To summarize, this paper presents a novel method to improve polarization conversion performance by utilizing ATS structures, and a metasurface with ATS is proposed based on this method. Ultimately, at $r = 5$ μm, for the ATS, the standard of PCR > 90% can be attained in the operating band of 0.90–1.86 THz. The RB at this point reached 69.6%, which met the evaluation criteria for ultra-broadband. In this paper, the polarization conversion principle is explained through equation derivation and surface current analysis. Furthermore, the angular stability and several essential parameters are also contrasted and debated in a targeted manner. The proposed metasurface has promising applications in radar, communications, and imaging technology.

Funding. Postgraduate Research & Practice Innovation Program of Jiangsu Province (KYCX22_0931).

Disclosures. The authors declare no conflicts of interest.

Data availability. Data underlying the results presented in this paper are not publicly available at this time but may be obtained from the authors upon reasonable request.

REFERENCES

1. X. Y. Yu, X. Gao, W. Qiao, and L. L. Wen, "Broadband tunable polarization converter realized by graphene-based metamaterial," IEEE Photon. Techol. Lett. **28**, 2399–2402 (2016).
2. B. Q. Lin, B. H. Wang, W. Meng, X. Y. Da, W. Li, Y. W. Fang, and Z. H. Zhu, "Dual-band high-efficiency polarization converter using an anisotropic metasurface," J. Appl. Phys. **119**, 183103 (2016).
3. E. Owiti, H. N. Yang, P. Liu, O. Calvine, and X. D. Sun, "Polarization converter with controllable birefringence based on hybrid all-dielectric-graphene metasurface," Nanoscale Res. Lett. **13**, 38 (2018).
4. J. D. Baena, J. P. D. Risco, A. Slobozhanyuk, S. B. Glybovski, and P. A. Belov, "Self-complementary metasurfaces for linear-to-circular polarization conversion," Phys. Rev. B **92**, 245413 (2015).
5. J. Y. Tang, Z. Y. Xiao, K. K. Xu, X. L. Ma, D. J. Liu, and Z. H. Wang, "Cross polarization conversion based on a new chiral spiral slot structure in THz region," Opt. Quantum Electron **48**, 111 (2016).
6. S. W. Luo, L. Bin, A. L. Yu, J. Gao, X. B. Wang, and D. L. Zuo, "Broadband tunable terahertz polarization converter based on graphene metamaterial," Opt. Commun. **413**, 184–189 (2018).
7. L. Zeng, H. F. Zhang, G. B. Liu, and T. Huang, "A three-dimensional linear-to-circular polarization converter tailored by the gravity field," Plasmonics **14**, 1347–1355 (2019).
8. W. L. Guo, G. M. Wang, K. Chen, H. P. Li, Y. Q. Zhuang, H. X. Xu, and Y. J. Feng, "Broadband polarization-conversion metasurface for a Cassegrain antenna with high polarization purity," Phys. Rev. Appl. **12**, 014009 (2019).
9. L. Zeng, H. F. Zhang, G. B. Liu, and T. Huang, "Broadband linear-to-circular polarization conversion realized by the solid state plasma metasurface," Plasmonics **14**, 1679–1685 (2019).
10. Z. C. Li, W. W. Liu, H. Cheng, S. Q. Chen, and J. G. Tian, "Realizing broadband and invertible linear-to-circular polarization converter with ultrathin single-layer metasurface," Sci. Rep. **5**, 18106 (2015).
11. X. F. Zang, S. J. Liu, H. H. Gong, Y. J. Wang, and Y. M. Zhu, "Dual-band superposition induced broadband terahertz linear-to-circular polarization converter," J. Opt. Soc. Am. B **35**, 950–957 (2018).
12. M. Chen, W. Sun, J. Cai, L. Chang, and X. Xiao, "Frequency-tunable mid-infrared cross polarization converters based on graphene metasurface," Plasmonics **12**, 699–705 (2017).
13. J. Zhou, J. Dong, B. Wang, T. Koschny, M. Kafesaki, and C. M. Soukoulis, "Negative refractive index due to chirality," Phys. Rev. B **79**, 121104 (2009).

14. J. Han, X. Cao, J. Gao, J. Wei, Y. Zhao, S. Li, and Z. Zhao, "Broadband radar cross section reduction using dual-circular polarization diffusion metasurface," IEEE Antennas Wireless Propag. Lett. **17**, 969–973 (2018).
15. X. X. Zheng, Z. Y. Xiao, and X. Y. Ling, "Broadband and efficient reflective polarization converter based on a three-dimensional metamaterial," Opt. Quantum Electron. **48**, 461 (2016).
16. Y. H. Ko, N. Razmjooei, and H. Hemmati, "Perfectly-reflecting guided-mode-resonant photonic lattices possessing Mie modal memory," Opt. Express **29**, 26971–26982 (2021).
17. S. Y. Wang, W. Liu, and W. Geyi, "A circular polarization converter based on in-linked loop antenna frequency selective surface," Appl. Phys. B **124**, 126 (2018).
18. W. Zhang, W. M. Zhu, E. E. M. Chia, Z. X. Shen, H. Cai, Y. D. Gu, W. Ser, and Y. D. Liu, "A pseudo-planar metasurface for a polarization rotator," Opt. Express **22**, 10446–10454 (2014).
19. N. Roudbarian, E. Jebellat, and S. Famouri, "Shape-memory polymer metamaterials based on triply periodic minimal surfaces," Eur. J. Mech. A **96**, 104676 (2022).
20. M. G. Wei, Q. Xu, Q. Wang, X. Q. Zhang, Y. F. Li, J. Q. Gu, Z. Tian, X. X. Zhang, J. G. Han, and W. L. Zhang, "Broadband non-polarizing terahertz beam splitters with variable split ratio," Appl. Phys. Lett. **111**, 071101 (2017).
21. Y. Jiang, L. Wang, J. Wang, C. N. Akwuruoha, and W. Cao, "Ultra-wide band high-efficiency reflective linear-to-circular polarization converter based on metasurface at terahertz frequencies," Opt. Express **25**, 27616–27623 (2017).
22. X. Gao, X. Han, W. P. Cao, H. O. Li, H. F. Ma, and T. J. Cui, "Ultra-wide band and high-efficiency linear polarization converter based on double V-shaped metasurface," IEEE Trans. Antennas Propag. **63**, 3522–3530 (2015).
23. Y. Z. Cheng, J. P. Fan, H. Luo, and F. Chen, "Dual-band and high-efficiency circular polarization convertor based on anisotropic metamaterial," IEEE Access **99**, 7615–7621 (2019).
24. X. Jing, X. C. Gui, P. W. Zhou, and Z. Hong, "Physical explanation of Fabry–Pérot cavity for broadband bilayer metamaterials polarization converter," J. Lightwave Technol. **36**, 2322–2327 (2018).
25. J. X. Zhao, B. X. Xiao, X. J. Huang, and Y. H. Lin, "Multiple-band reflective polarization converter based on complementary L-shaped metamaterial," Microw. Opt. Technol. Lett. **57**, 978–983 (2015).
26. J. M. Hao, Y. Yuan, L. X. Ran, T. Jiang, J. A. Kong, C. T. Chan, and L. Zhou, "Manipulating electromagnetic wave polarizations by anisotropic metamaterials," Phys. Rev. Lett. **99**, 063908 (2007).
27. N. K. Grady, J. E. Heyes, D. R. Chowdhury, Y. Zeng, M. T. Reiten, A. K. Azad, A. J. Taylor, D. A. R. Dalvit, and H. T. Chen, "Terahertz metamaterials for linear polarization conversion and anomalous refraction," Science **340**, 1304–1307 (2013).
28. Y. M. Yang, W. Y. Wang, P. Moitra, I. I. Kravchenko, D. P. Briggs, and J. Valentine, "Dielectric meta-reflectarray for broadband linear polarization conversion and optical vortex generation," Nano Lett. **14**, 1394–1399 (2014).
29. L. Zhang, P. Zhou, H. Lu, L. Zhang, J. Xie, and L. Deng, "Realization of broadband reflective polarization converter using asymmetric cross-shaped resonator," Opt. Mater. Express **6**, 1393–1404 (2016).
30. J. C. Zhao, Y. Z. Cheng, and Z. Z. Cheng, "Design of a photo-excited switchable broadband reflective linear polarization conversion metasurface for terahertz waves," IEEE Photon. J. **10**, 4600210 (2018).
31. R. T. Ako, W. S. L. Lee, M. Bhaskaran, S. Sriram, and W. Withayachumnankul, "Broadband and wide-angle reflective linear polarization converter for terahertz waves," APL Photon. **4**, 096104 (2019).
32. Y. P. Li, H. F. Zhang, and T. Yang, "Realizing ultra-bandwidth cross-polarization conversion by a double-layer metasurface," J. Opt. Soc. Am. B **37**, 3572–3580 (2020).
33. X. L. Zhang, H. N. Ye, Y. Zhao, and H. Zhang, "A tunable ultra-wideband cross-polarization conversion based on the band splicing technology," Appl. Phys. B **127**, 69 (2021).
34. W. Huang, X. Y. Hao, Y. Cheng, S. Yin, J. G. Han, and W. T. Zhang, "Broadband terahertz half-wave plate with multi-layered metamaterials designed via quantum engineering," J. Lightwave Technol. **39**, 7925–7929 (2021).
35. C. R. Liu, J. H. Wu, X. Chen, and F. Y. Ma, "A thin low-frequency broadband metasurface with multi-order sound absorption," J. Phys. D **52**, 105302 (2019).
36. H. Zhang, Y. Ma, and H. F. Zhang, "Band enhanced ultra-broadband terahertz absorber based on a high-impedance surface and cavity resonance," Appl. Opt. **57**, 9208–9214 (2018).
37. G. Armelles, B. Caballero, A. Cebollada, A. G. Martin, and D. M. Rodríguez, "Magnetic field modification of optical magnetic dipoles," Nano Lett. **15**, 2045–2049 (2015).
38. R. Magnusson, K. L. Lee, and H. Hemmati, "Properties of resonant photonic lattices: Bloch mode dynamics, band flips, and applications," Proc. SPIE **11290**, 1129006 (2020).
39. Y. Q. Hu, X. D. Wang, X. H. Luo, X. N. Ou, L. Li, Y. Q. Chen, P. Yang, S. Wang, and H. G. Duan, "All-dielectric metasurfaces for polarization manipulation: principles and emerging applications," Nanophotonics **9**, 3755–3780 (2020).
40. Y. D. Deng and Z. Y. Song, "Manipulating polarization and electromagnetically induced transparency in a switchable metamaterial," Opt. Mater. **105**, 109972 (2020).
41. R. M. Gao, Z. C. Xu, C. F. Ding, L. Wu, and J. Q. Yao, "Graphene metamaterial for multiband and broadband terahertz absorber," Opt. Commun. **356**, 400–404 (2015).
42. L. X. Liu, X. Q. Zhang, M. Kenney, X. Q. Su, N. N. Xu, C. M. Ouyang, Y. L. Shi, J. G. Han, W. L. Zhang, and S. Zhang, "Broadband metasurfaces with simultaneous control of phase and amplitude," Adv. Mater. **26**, 5031–5036 (2014).
43. R. T. Ako, A. Upadhyay, W. Withayachumnankul, M. Bhaskaran, and S. Sriram, "Dielectrics for terahertz metasurfaces: material selection and fabrication techniques," Adv. Opt. Mater. **8**, 1900750 (2020).